BBAA VI International Colloquium on:
Bluff Bodies Aerodynamics & Applications
Milano, Italy, July, 20–24 2008

3D FLOW AROUND A RECTANGULAR CYLINDER: A COMPUTATIONAL STUDY

Luca Bruno***, Davide Fransos**†**, Nicolas Coste**‡ **and Arianna Bosco***

* Dipartimento di Ingegneria Strutturale e Geotecnica
Politecnico di Torino, Viale Mattioli 39, 10126 Torino, Italy
e-mail: luca.bruno@polito.it

† Dipartimento di Matematica
Politecnico di Torino, Corso Duca degli Abruzzi 24, 10129 Torino, Italy
e-mail: davide.fransos@polito.it

‡ OptiFlow Company
Hôtel Technologique B.P. 100, Technopôle de Château Gombert, 13382 Marseille, France
e-mail: coste@optiflow.fr

* Aachen Institut for advanced studies in Computational Engineering Science
RWTH Rheinisch-Westflische Technische Hochschule Aachen, Pauwelstrasse 12, 52074 Aachen, Germany
e-mail: bosco@aices.rwth-aachen.de

Keywords: Computational Wind Engineering, Large Eddy Simulation, rectangular cylinder

Abstract: *The aim of this paper is to provide a contribution to the study of the 3D, high Reynolds number, turbulent, separated and reattached flow around a fixed rectangular cylinder with a chord-to-depth ratio of 5. In spite of the simple geometry, it is believed that the problem could be of interest not only for fundamental research purposes, but also to provide useful information on the aerodynamics of a wide range of bluff bodies of interest in Civil Engineering (e.g. long span bridge decks, high-rise buildings, and so on) and in other Engineering applications. First, the obtained main aerodynamic integral parameters are compared with those proposed in literature. Second, the 3D features of the flow are investigated by means of both Proper Orthogonal Decomposition and coherence function of the side-surface fluctuating pressure field. Once the main 2D nature of the flow has been pointed out, some of the 2D mechanisms that are responsible for the variation of the fluctuating aerodynamic forces are scrutinised: the computational approach post-processing facilities are employed to look for significant relationships between the flow structures, pressure field and aerodynamic forces.*

1 INTRODUCTION

The aerodynamic behaviour of rectangular cylinders has attracted the attention of the scientific community since the experimental reference works of Okajima [1] and Norberg [2]. On one hand, both the two dimensional (2D) and three dimensional (3D) features of the low-Reynolds number flow around rectangular cylinders has been clarified in several studies (e.g. [3, 4, 5]). On the other hand, the high-Reynolds number flow (i.e. $Re \geq 1.e + 4$) has been studied by means of both experimental and computational approaches, with emphasis on its dependence on the chord-to-depth ratio [6, 7, 8]. In particular, $Re = 4.e + 4$ has been adopted in the present study, while the chord-to-depth ratio has been set equal to 5 as a representative benchmark of a bridge deck or high-rise building elongated section. Its ratio is far enough from those at which discontinuities in the aerodynamic regime arise, i.e. the 2.8 and 6 ratios [8], in order to avoid the introduction of further difficulties in the study.

Two main aspects are focused on in the study. First, the evaluation of the 3D features of the flow around nominally 2D bluff cylinders remains an inescapable task also for rectangular sections. Studies through both experimental [9] and computational [10] approaches have contributed to this topic in the case of rectangular cylinders. Apart from the span-wise correlation coefficient [11] and the coherence spectral function [9], which are generally employed for long cylinders, the Proper Orthogonal Decomposition (POD) methodology is being adopted more and more for the analysis and synthesis of random wind pressure fields. Even though POD has been traditionally applied to high-rise buildings [12, 13, 14], an application to rectangular cylinders was proposed in [15] and used in the present work to quantify the 3D flow features. Second, according to the authors, some difficulties remain in describing the expected complex flow phenomena around a cylinder and in relating such phenomena to the fluctuating aerodynamic forces acting on the cylinder itself: the computational approach post-processing facilities are here employed to look for significant relationships between flow structures, pressure field and aerodynamic forces.

2 FLOW MODELLING AND COMPUTATIONAL APPROACH

The 3D, turbulent, unsteady flow around the cylinder is modelled in the frame of the Large Eddy Simulation approach to turbulence using the classical time-dependent filtered Navier-Stokes equations

$$\frac{\partial \overline{u_i}}{\partial x_i} = 0, \tag{1}$$

$$\frac{\partial \overline{u_i}}{\partial t} + \frac{\partial \overline{u_i}\ \overline{u_j}}{\partial x_j} = -\frac{1}{\rho}\frac{\partial \overline{p}}{\partial x_i} + \frac{\partial}{\partial x_j}\left[\nu\left(\frac{\partial \overline{u_i}}{\partial x_j} + \frac{\partial \overline{u_j}}{\partial x_i}\right) + \tau^s_{ij}\right], \tag{2}$$

where ν is the kinematic viscosity and $\overline{u}$ and $\overline{p}$ are the filtered velocity and pressure, respectively. The sub-grid stress tensor is expressed according to Boussinesq's assumption as

$$\tau^s_{ij} = \nu_t\left(\frac{\partial \overline{u_i}}{\partial x_j} + \frac{\partial \overline{u_j}}{\partial x_i}\right), \tag{3}$$

so that the equation system can be closed by a transport equation for the kinetic energy k_t of the unresolved stresses [16]

$$\frac{\partial k_t}{\partial t} + \frac{\partial}{\partial x_j}(\overline{u_j}k_t) = \frac{\partial}{\partial x_j}\left[(\nu + \nu_t)\frac{\partial k_t}{\partial x_j}\right] + P_k - C_\epsilon\frac{k_t^{3/2}}{l_\epsilon}, \tag{4}$$

where $P_k = 2\nu_t \overline{S_{ij}}\ \overline{S_{ij}},\ \nu_t = C_k l_k k_t^{1/2}$, the constants are set equal to $C_\epsilon = 1.05$, $C_k = 0.07$ and $l_\epsilon = l_k = \Delta$, and Δ is the characteristic spatial length of the filter. The subgrid k_t equation is damped approaching the wall as $\nu_t = \sqrt{u_\tau/U}$, where u_τ is the tangential velocity component and U is the free stream velocity.

The computational domain and the boundary conditions are shown in Figure 1. The spanwise length of the domain is equal to $L/B = 1$. Dirichlet conditions on the velocity field and

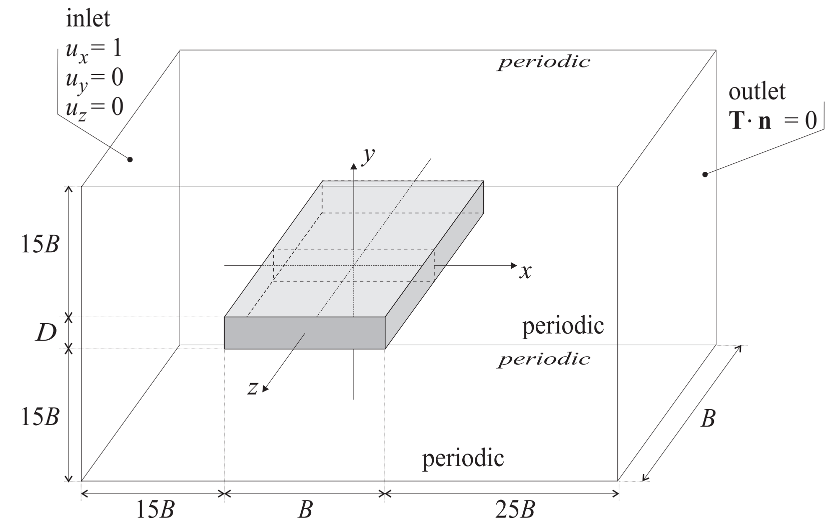

Figure 1: Analytical domain and boundary conditions

on the sub-grid kinetic energy are imposed at the inlet boundaries. Neumann conditions on the normal component of the stress tensor **T**, as well as the same Dirichlet conditions on k_t, are imposed at the outlet boundaries. Periodic conditions are imposed on both the side surfaces and on the upper-lower surfaces, as depicted in Figure 1. No-slip conditions are imposed at the section surface. The initial conditions are obtained from a previous LES simulation, where the standard Smagorinsky sub-grid model [17] was employed.

A hexahedral grid is adopted to discretise the spatial computational domain. A body-fitted, structured boundary layer grid is generated near the wall and a paved hexahedral grid is used to fill the remaining part of the domain. The computational grid in space consists of about 6.33×10^6 cells. The resulting non-dimensional mean wall distance value y^+ is close to the unit. The non-dimensional time-step needed for an accurate advancement in time is $\Delta t = 5 \times 10^{-3}\ tU/D$. The simulation is extended over $T = 800\ tU/D$ non dimensional time units in order to overcome the transient solution and to allow the statistical analysis of the periodic flow.

The OpenFoam Finite Volume open source code is used in the following to numerically evaluate the flow-field. The cell-centre values of the variables are interpolated at face locations using the second-order Central Difference Scheme for the diffusive terms and the Limited Linear scheme for the convection terms [18]. Advancement in time is accomplished by the two-step Backward Differentiation Formulae (BDF) method. The pressure-velocity coupling is achieved by means of the pressure-implicit PISO algorithm, using a predictor-corrector approach for the time discretisation of the momentum equation, whilst enforcing the continuity equation.
Computations are carried out on 8 Intel Quadcore X5355 2.66GHz CPUs and require about 2.5GB of memory and 15 days of CPU time for the whole simulation.

3 APPLICATION AND RESULTS

The incoming flow is characterised by a $Re = UD/\nu = 4.e+4$ Reynolds number, an incidence $\alpha = 0$ and a turbulence intensity $It = 0\%$ (ideal smooth flow). The cylinder rectangular cross section is characterised by sharp edges and smooth surfaces.

3.1 Integral Parameters

The main aerodynamic integral parameters are analysed in this section in order to define an efficient time windowing for the statistical study of all the flow features, and to roughly collocate the present results in the large number of data available in literature about pressure forces and wake frequencies for this section. According to the authors, more accurate and point-wise comparisons, especially for CFD validation purposes, are hard propose at present because of the incomplete information about the experimental or computational set-up in each study. The mean value and the standard deviation of the drag coefficient $C_D = F_D/(1/2\rho UD)$ and lift coefficient $C_L = F_L/(1/2\rho UD)$ are retained. The Strouhal number $St = f_1 D/U$ is evaluated from the heuristic analysis of the lift spectrum, where f_1 is the dominant frequency.
The extent of the sampling window is a key and critical element for the extraction of meaningful statistical parameters in the CFD approach, due to the computational costs involved in long physical time simulations. Figure 2(a) shows the time histories of the drag and lift coefficients. The transient solution, due to the initial conditions, covers the first 150 non dimensional time units tU/D, which are discarded. In order to optimise the sampling extent during the stationary

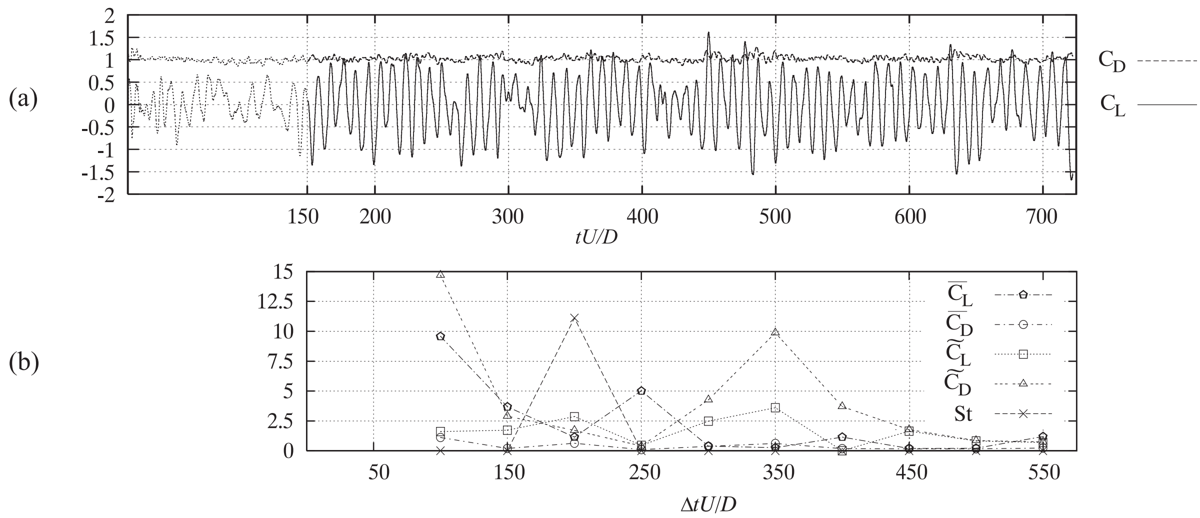

Figure 2: Time histories of the drag and lift coefficients (a) and convergence of the related statistics (b)

regime, the convergence of the mean values and standard deviations of the drag and lift coefficients are checked, as for the Strouhal number, for increasing extents of the sampling window (Figure 2(b)). A non dimensional sampling extent $\Delta tU/D \geq 400$ has been found to be required to avoid a larger error than 5% in the statistical first moments. In the following, $\Delta tU/D = 500$ is retained, which corresponds to around 60 vortex-shedding periods.
Figure 3 compares the present results with experimental and computational data collected in [8] and with the results obtained in [7]. The obtained mean drag coefficient $\overline{C}_D$ and St number are in good agreement with the other data obtained at the same chord-to-depth ratio and they are in accordance with the general parameter trend versus the B/D ratio. Some results

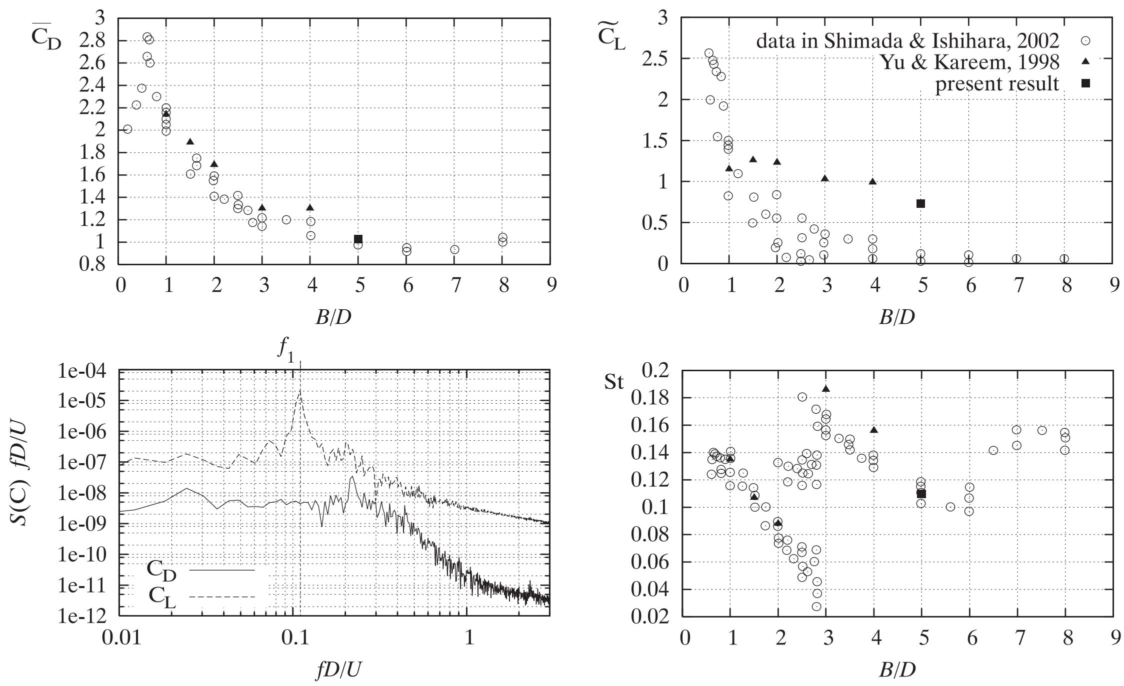

Figure 3: Mean drag and rms lift coefficients, Strouhal number: comparison with results from literature

from literature concerning the standard deviation of the lift coefficient show a significant dispersion: in particular, the higher the B/D ratio, the higher the differences among the results. The reasons for the above mentioned dispersion are not completely clear: the expected parameter sensitivity to physical incoming flow conditions (e.g. Re number, turbulence intensity and integral length scale), experimental set-up conditions and/or computational model components (e.g. turbulence modelling, numerical approaches) could be systematically addressed in future research. For now, it can be noticed that the present 3D LES result is in agreement with the trend obtained by Yu and Kareem [7], who used the same approach, while Shimada and Ishihara [8] pointed out a significant underestimation of the fluctuating force components in most of the RANS models.

3.2 3D Flow Features

The main aim of this section is to evaluate whether 3D flow features exist around a nominally 2D rectangular cylinder, where 3D effects take place and in which way they contribute to the overall flow dynamics. Figure 4 shows the instantaneous vorticity field around the obstacle. From a qualitative point of view, 3D flow structures clearly appear even though the 2D main flow field remains. Generally speaking, the further the location from the separation point at the leading edge, the more significant the 3D features of the flow structures. In particular, the flow seems almost 2D just downstream from the separation point, while the wake structure is clearly 3D.

The fluctuating pressure field on the upper side-surface is analysed in order to quantitatively evaluate the role played by the 3D flow structure on the lift force. The analysis employes both the POD methodology, to uncover any deterministic structures dominating the field and to discuss their 2D/3D nature, and the span-wise coherence, to clarify the mechanism of the high coherent structures, i.e., the 2D ones.

The POD analysis is performed on a 5000-point structured grid (200 points along the x direction

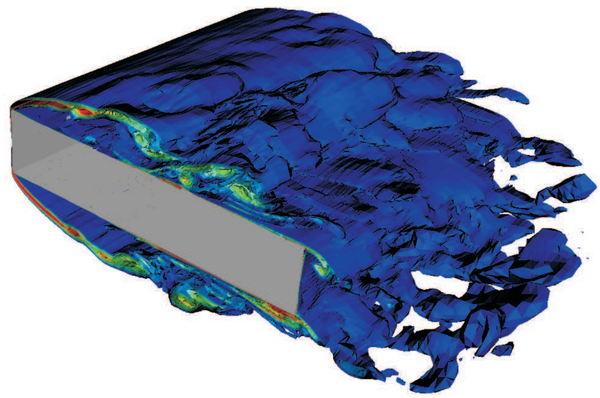

Figure 4: 3D instantaneous vorticity magnitude iso-surface ($\omega \geq 20$)

and 25 points along the z direction). The non dimensional sampling time is equal to $\Delta t_{POD} = 2.5 \times 10^{-2}\ tU/D$, the sampling window is equal to $T_{POD} = 500\ tU/D$. The mode extraction requires 15.8 Gb of memory. A 3D indicator is proposed for the i-th eigenvector $\Phi_i(x, z)$, in order to assess the 2D/3D nature of each mode in a compact form, as the along-x average of the along-z standard deviation $\phi_i = mean_x(std_z(\Phi_i))$. Figure 5(a) graphs the ratio ϕ_i/ϕ_{max} for $1 \leq i \leq 40$. The first two modes are associated with very low values of the ratio $\phi/\phi_{max} \leq 0.1$,

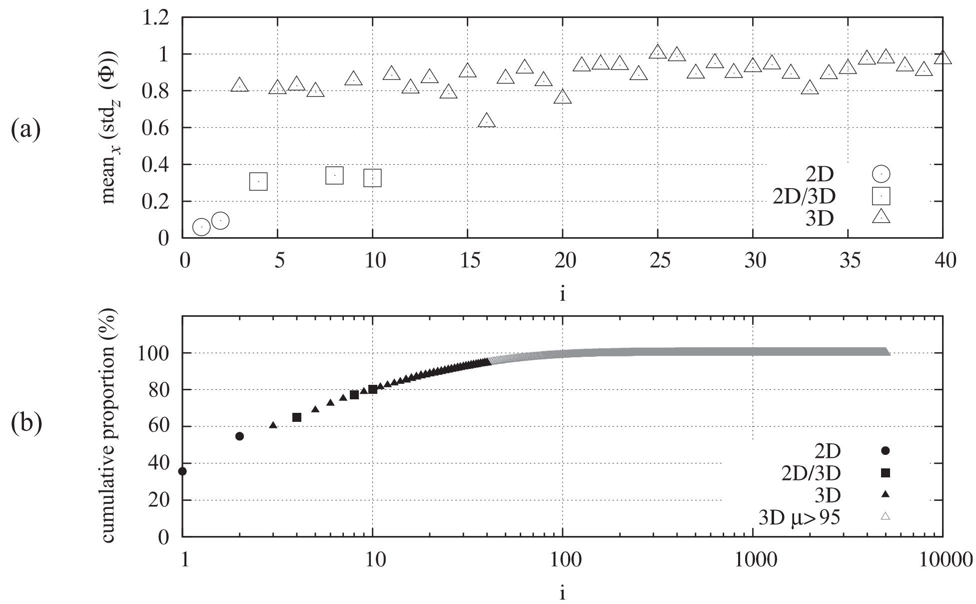

Figure 5: Proper Orthogonal Decomposition: (a) eigenvector 3D indicator and (b) eigenvalue cumulative proportion

and can therefore mainly be considered as 2D, as can be easily seen in Figure 6. The 4th, 8th and 10th eigenvectors have intermediate ϕ values ($0.3 \leq \phi/\phi_{max} \leq 0.4$), and cannot therefore be ascribed to either the 2D or to the 3D ones. Finally, the other eigenvectors show high values of the ratio $\phi/\phi_{max} \geq 0.6$, having significant 3D trends. The 3rd to the 10th eigenvectors are represented in Figure 7.

The two first modes, i.e. the 2D ones, are qualitatively similar to the ones obtained in [15] through a 2D LES. Their shape seems to be connected to the vortex convection along the side surface of the cylinder. All the modes are almost constant and 2D in a zone which is approx-

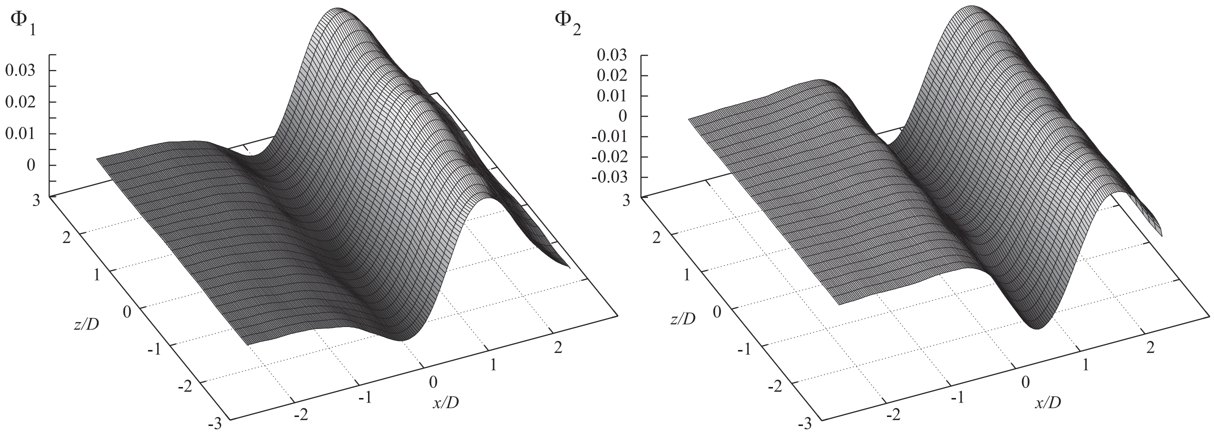

Figure 6: Proper Orthogonal Decomposition: 2D eigenvectors

imately $1.5D$ long in the x direction just downstream from the leading edge. Some of the 3D modes, namely Φ_3, Φ_5 and Φ_7, show an antisymmetric variation in the z direction, whose characteristic scale is about L, i.e. the span-wise dimension of the computational domain. Other 3D modes, e.g. Φ_6, show variations in the z direction which are more than L long. This suggests further parametrical studies on the span-wise domain dimension, compatibly with the required computational cost.

The cumulative eigenvalue proportion is plotted in Figure 5(b), where each mode is once more classified according to its prevailing 2D or 3D feature. The overall 2D mode contribution is equal to 54.7%, where the 1st mode contributes 35.63% and the 2nd mode 19%. The 2D/3D modes contribute 8.2%, while the 3D ones contribute 37.1%. It is worth pointing out that the cumulative proportion up to the 40th mode is 95%, while there is a total of 5000 modes. This means that about 0.8% of the modes can reproduce a relatively detailed structure of the wind pressure fluctuations acting on each point of the side surface within an error of around 5%.

The coherence of the surface pressure in the span-wise direction is taken into account as a further way of highlighting the high coherent (i.e., 2D) structures of the flow. The coherence function of the surface pressure is expressed as

$$\text{coh}(\Delta z; \overline{p}) = \frac{|S(\Delta z; \overline{p})|}{\sqrt{S_{z=0}(\overline{p})}\sqrt{S_{z=\Delta z}(\overline{p})}}, \tag{5}$$

where $S(\Delta z; \overline{p})$ is the cross spectrum with the span-wise separation of Δz and $S_{z=0}(\overline{p})$ and $S_{z=\Delta z}(\overline{p})$ are the power spectra at $z = 0$ and $z = \Delta z$, respectively. Figure 8 shows the obtained coherence functions at the $x/D = -1.59$ and $x/D = 1.59$ locations for different Δz values. The results are compared to those of the wind tunnel test reported in [9]. The present results are characterised by a lower frequency resolution, due to a smaller length of the time sample than that of the wind tunnel test. High coherence peaks are present in all the cases in correspondence to the St number, in agreement with the experimental results, which, however, show narrower peaks. The coherence decays outside the Strouhal region as the span-wise distance grows. This seems to confirm the previously stated bound between the vortex convection and the main 2D flow characteristics. The same coherence function is computed at four different x/D locations and plotted in Figure 9, in order to identify the different coherence behaviour along the cylinder lateral surface. High coherence around the St number and a coherence decaying with Δz in the other frequency ranges are present at $x/D = -2.4749$ and $x/D = 1.2437$, similarly to

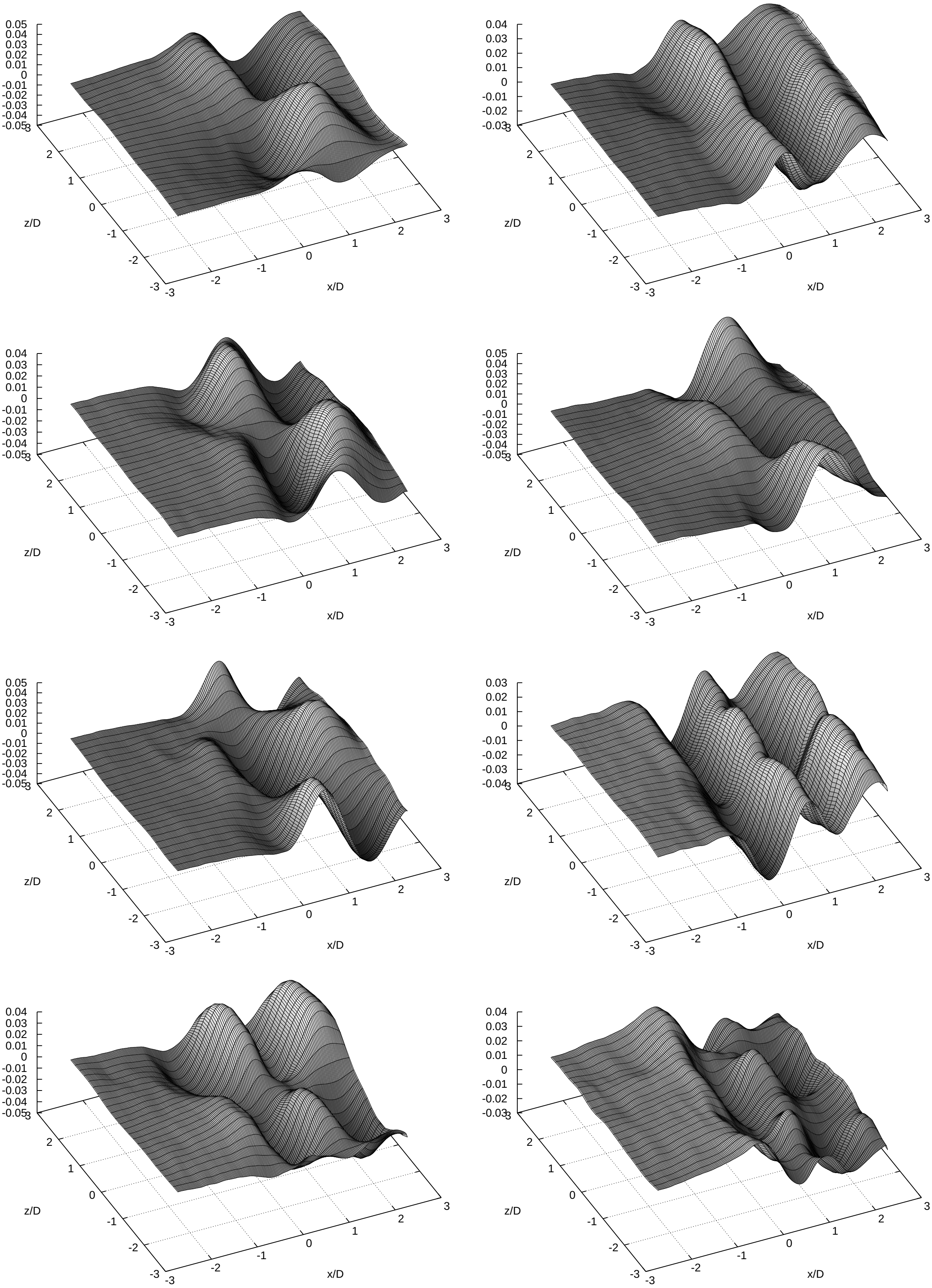

Figure 7: Proper Orthogonal Decomposition: eigenvectors from 3 to 10 in lexicographic order

the previous cases. A more homogeneous behaviour is highlighted at $x/D = -0.2638$ and $x/D = 2.4749$, suggesting the need to investigate the different physical phenomena which prevail in different zones of the lateral surface.

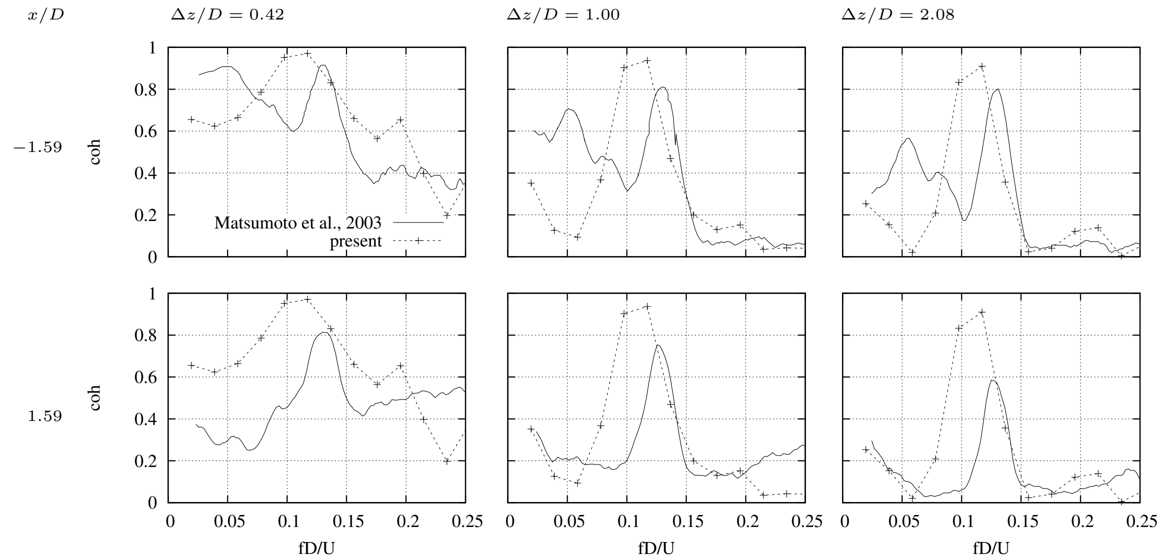

Figure 8: Coherence functions: comparison with results by Matsumoto et al., 2003

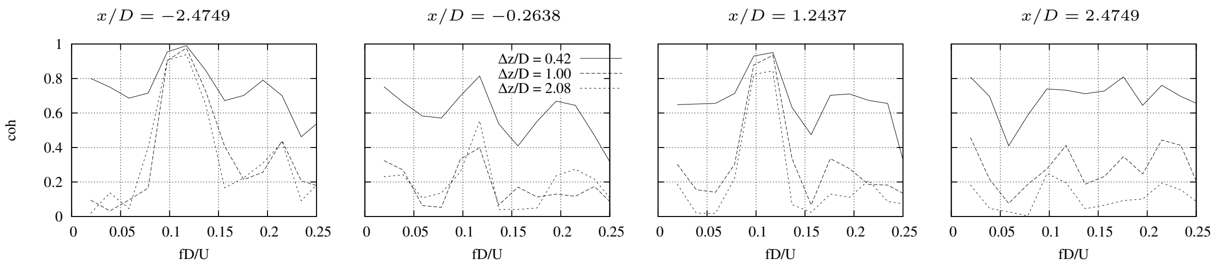

Figure 9: Coherence functions at different locations along the upper lateral surface

3.3 2D Flow Features

In order to focus on the 2D flow phenomena that mainly affect the aerodynamic behaviour of the cylinder, the main mean flow structures in the central section $z/D = 0$ are pointed out and discussed first. Second, some 2D instantaneous flow fields are sampled to point out some of the main mechanisms that are responsible for the fluctuating pressure and aerodynamic force variation.

The topology of the symmetric mean flow around the obstacle is shown in Figure10: the mean velocity vectors are plotted in the upper part of the figure, while a synthetic scheme of the recognised flow structure is proposed in the lower part. A pseudo-triangular region can be recognised downstream from the separation point at the upwind edges, analogously to what has already experimentally been observed by Pullin & Perry and numerically simulated by Braza et al. [19]. A bubble and a secondary eddy can be distinguished inside this region. The mean vortex shed from the apex of this region shows an inclined major axis. The mean flow reattaches just upstream from the trailing edge.

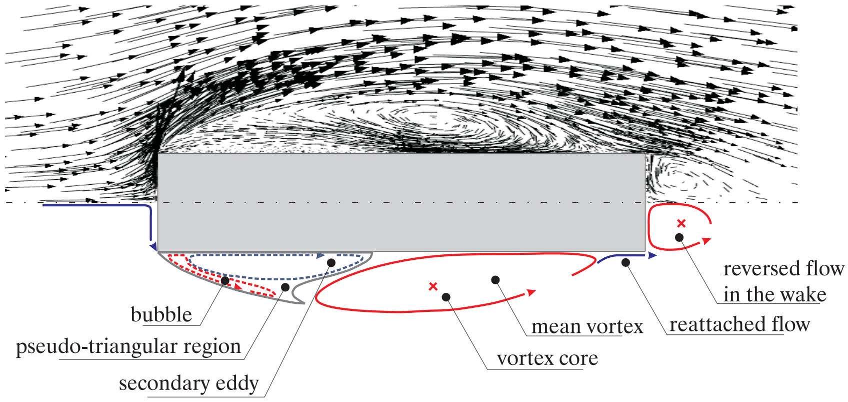

Figure 10: Mean velocity field and schematised flow structures in the central section

The mean wall shear stress coefficient $\overline{C}f$ distribution on the lower half perimeter is plotted in Figure 11(a) and referred to the mean flow structures discussed above. The changes in sign of $\overline{C}f$ permit the x-length of the four structures along the side surface to be measured: counter-clockwise flow structures (separation bubble and main vortex) give rise to a negative $\overline{C}f$, while the clockwise secondary eddy and the reattached flow involve positive values. The sum of the pseudo-triangular region and mean vortex lengths gives the distance of the reattaching point from the separation one. It follows that the overall non dimensional separation bubble length is equal to $x_R/B = 0.933$, which is larger than the one estimated by Matsumoto et al. [9] based on the distributions of the time averaged pressure coefficient and rms value. This slight discrepancy can be ascribed to the different identification methods that were adopted, but another possible explication can be found looking at the difference between the present incoming flow conditions (ideal smooth flow) and the experimental ones affected by wind tunnel residual incoming turbulence (see for instance [20, 21, 22]). Deeper studies would be required to verify this hypothesis.

Figures 11 (b)-(c)-(d) graph the distributions of the pressure mean value, standard deviation and skewness, respectively. In this case, an attempt is made to relate the trend of the Cp moments to the approximate extent of the main flow structures evaluated at the external boundary of the separating shear flow. Four regions result and these are named, quoted and graphically represented with grey patterns in the figure. It is worth recalling that the rigourous identification of the x-length of these zones, even though possible, is not the scope of this work, while approximate but phenomenon-based lengths have been preferred to make a guess at the relationship between the fluid flow phenomena and the aerodynamic forces.

The "separation bubble" (*sb*) region is defined as the x-distance from the separation point to the apex of the pseudo-triangular region and it is characterised by a $\overline{C}p$ plateau and low $\tilde{C}p$ values. The mean vortex x-length is split into two zones in order to distinguish the part of the side surface where the instantaneous vortex is shed and the one where the instantaneous reattachment takes place: the watershed point between these regions is obtained not only by looking at the point where the vortex-induced reversed flow at the wall has a non null vertical component, but also remembering the critical aspect ratio $B/D = 3$ that distinguishes separated-type and reattached-type rectangular sections. The "vortex-shedding" (*vs*) zone shows the maximum value of the mean suction and a steep increase of the fluctuating component, while the mean pressure recovery gives the name to the second region (*pr*), where the maximum rms value also occurs. The "mean reattachment flow" (*rf*) region is regained from above and is characterised

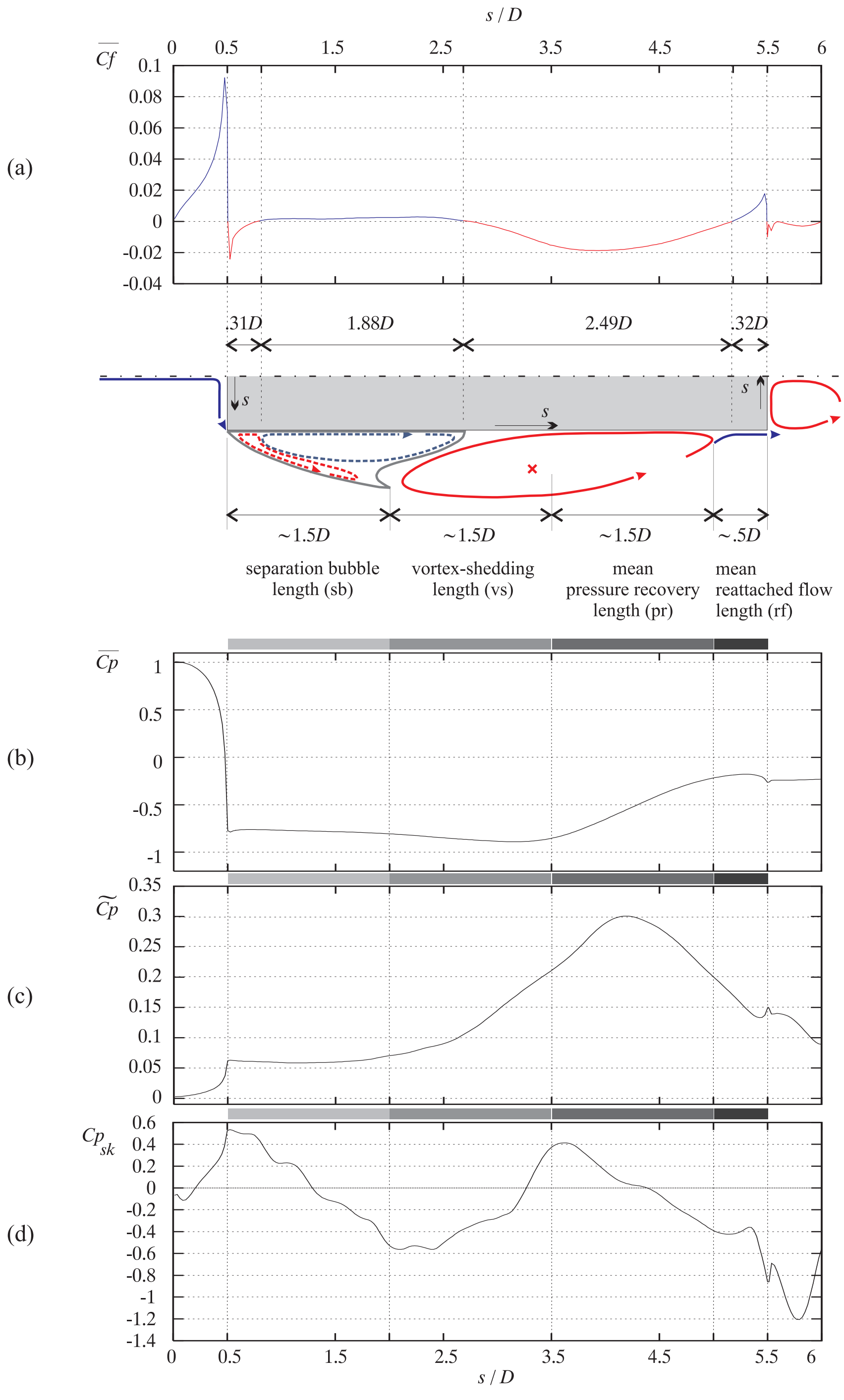

Figure 11: Flow structures, surface mapping, friction and pressure coefficient distributions along the central section

by another $\overline{Cp}$ plateau. Finally, it is worth pointing out that the longest lengths show a change in sign of the pressure skewness and that the bound of each length corresponds to its relative maximum or minimum values. Although longer sampling times are required to confirm this result and deeper studies are needed to interpret them, the features of the Cp_{sk} distribution seems to confirm the significance of the chosen points.

The same partition of the side-surface applies to the spectral content of the pressure signals: a window of the Cp time histories at the mid point of each length and the normalised PSDs along the side surface are plotted in Figure 12. The pressure fluctuations in the *sb* and *pr* lengths

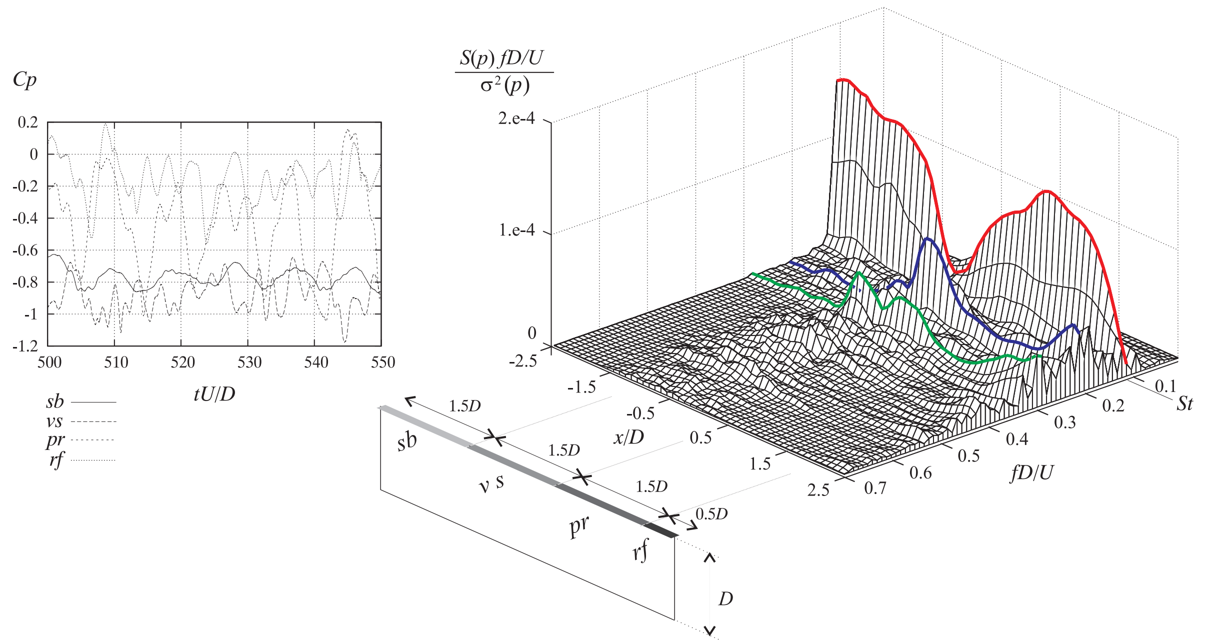

Figure 12: Pressure time histories and Power Spectral Density along the upper side surface

are mainly characterised by one frequency component, which corresponds to the prevailing frequency in the lift coefficient (St number). On the contrary, the points in the *vs* and *rf* lengths show a broad band spectrum, where the most significant frequencies are higher than St. It is worth recalling that these results are in agreement with the previously shown ones in Figures 8 and 9: the four points along the side surface correspond to the regions introduced in this section and the evaluated coherence functions at the abscissa $x/D = -0.2638$ and $x/D = 2.4749$ (in *vs* and *rf* lengths respectively) show low values along a broader frequency range than the point belonging to the *sb* and *pr* lengths. The largest pressure fluctuations along the *pr* length (Figure 11(c)) and its narrow spectral content close to St (Figure 12) seem to suggest that this region contributes to the lift fluctuation component to the greatest extent. This is in agreement with the conclusions drawn by Matsumoto et al. in [9].

In order to verify this hypothesis, Figure 13 gives an example of the attempt made to relate the instantaneous lift coefficient $C_L(t)$ to the instantaneous flow field, described by the vorticity magnitude contours around the central section and by the pressure distribution along the four regions in which the side surfaces have been partitioned. Four instants, corresponding to null, maximum, null and minimum values of the lift coefficient, have been retained for sampling. The $(+)$ sign in the instantaneous vorticity magnitude fields corresponds to counter-clockwise eddies, while the $(-)$ sign refers to clockwise ones. The suction peaks in the Cp distributions clearly correspond to the travelling vortices alternatively shed from the leading-edge and convected along the side surfaces. In spite of their magnitude, the suctions at the upper and lower side surfaces approximately cancel each other, and no significant effects on the net lift force arise. Positive pressure is recovered along part of the *pr* lengths at the lower and upper side surfaces and it involves the maximum and minimum lift values, respectively. This positive pressure recovery takes place at the time in which a new vortex is shed from the *vs* length and the previous one is already convected in the wake. In other words, the instantaneous pressure recovery grows in the time and space domains in between two consecutive vortices shed from the leading edge. At the same time, the *pr* length along the opposite side surface is submitted to a deep

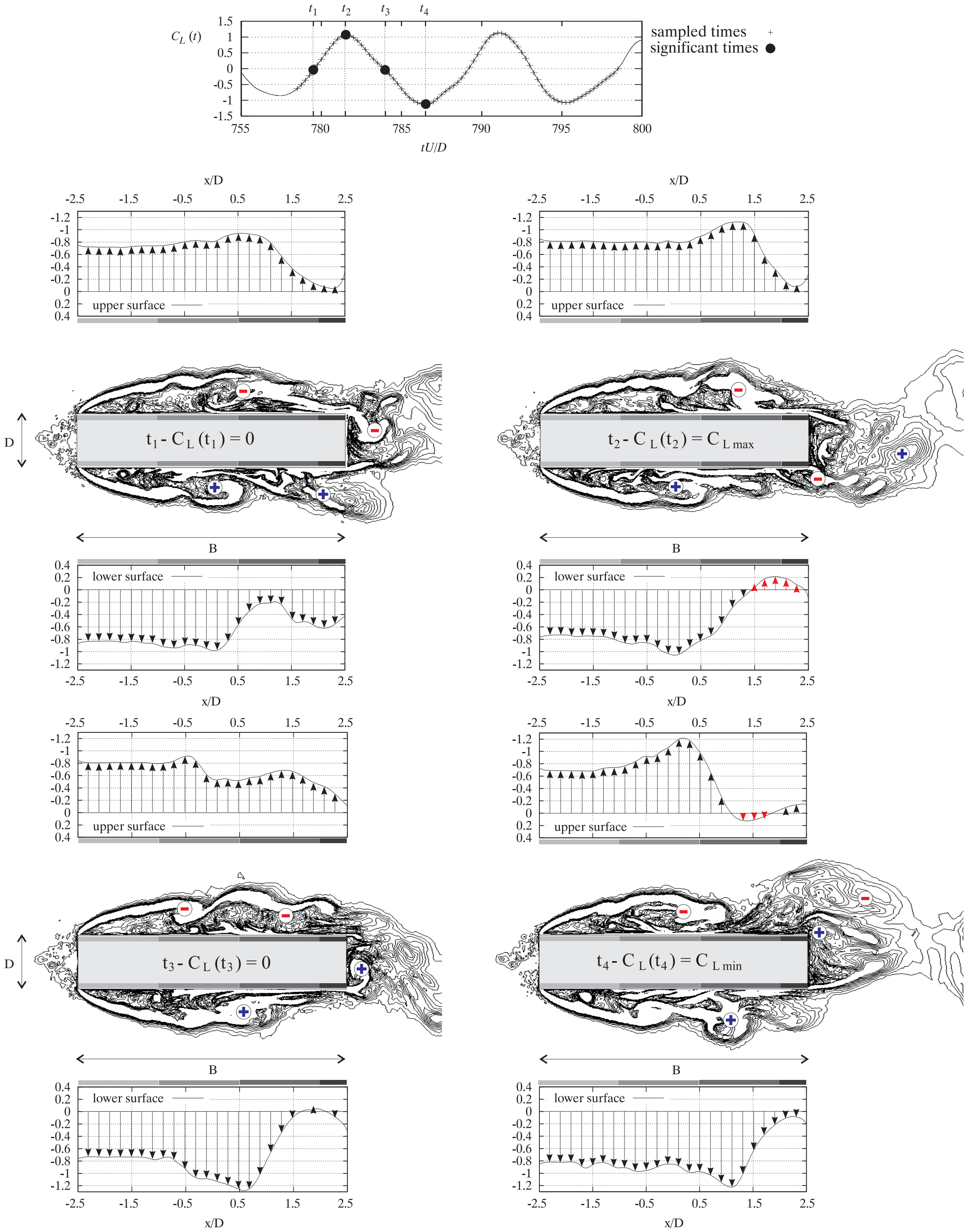

Figure 13: Instantaneous vorticity field and pressure distribution along a vortex-shedding period

suction due to the vortex travelling along it. Hence, the pressure resultant forces at the upper and lower *pr* lengths do not cancel each other as they have the same direction. The pressure-induced net lift force acting on the *pr* length predominates over the contribution of the other regions to the overall lift acting on the whole section, as Figure 14 demonstrates. Nevertheless,

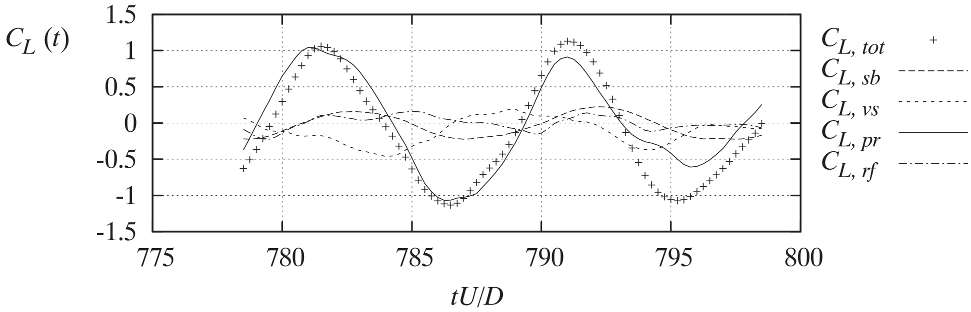

Figure 14: Net lift components expressed by the identified lengths

it is important to point out that the described mechanism is not the only one that is responsible for the aerodynamic behaviour of the cylinder, as the irregular lift time history suggests (Figure 2(a)). The same lift time history sampled in Figure 14 confirms this hypothesis at $tU/D \approx 795$, when the *pr* contribution alone is not enough to reconstruct the total lift force. According to the authors, further analysis would be required to identify complementary flow phenomena and to order them according to their contribution to the overall aerodynamic behaviour.

An example of this approach is given looking at the vortices shed from the section trailing edges and at their interaction with the leading vortices responsible for the previously described main mechanism. A schematic sketch of the proposed resulting mechanism is given in Figure 15 based on the simulated flow fields in Figure 13. The capital letter V refers to the vortices

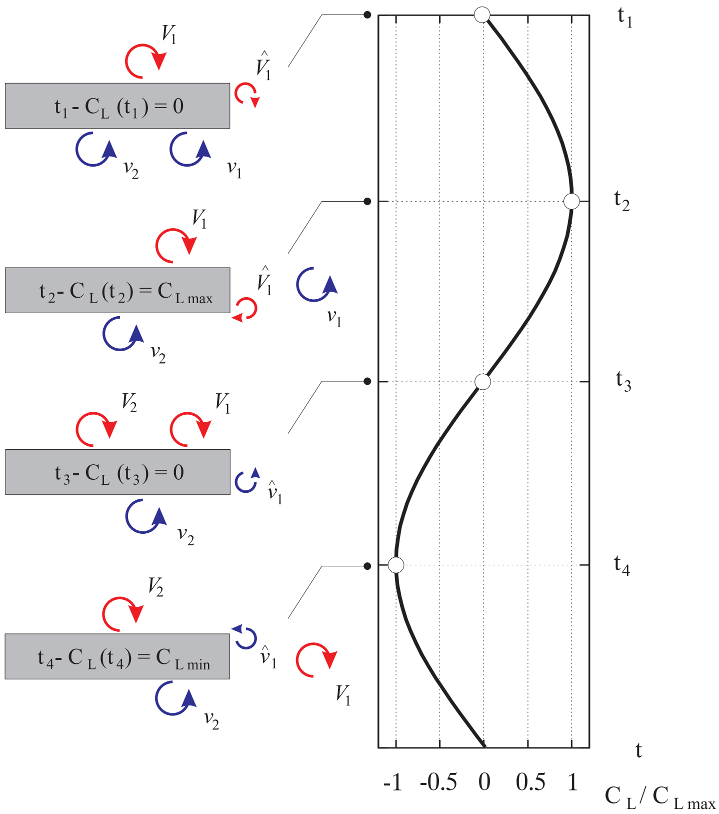

Figure 15: Schematised vortex locations over a vortex-shedding period

shed from the leading edge at the upper side surface, while the v symbol is adopted for the same vortices at the lower surface. The hat accent indicates vortices shed from the trailing edges. The instantaneous vorticity magnitude fields in Figure 13 show that, in correspondence to null lift, the vortices are shed from the trailing edges towards the centreline of the wake. These vortices can in fact travel across the whole wake and reach the opposite trailing edge: this happens when the vertical component of their convection velocity is not reduced by the velocity field induced by the vortex shed in the wake from the leading edge. In other words, if a trailing vortex can insert itself between two successive vortices convected along the opposite side surface, it can reach the trailing edge of the latter, slow down the incoming upstream vortex and induce a more extended instantaneous reattachment of the boundary layer and a stronger pressure recovery, as at t_2.

4 CONCLUSIONS

A computational study has been proposed in this work to analyse the main flow features of the high Reynolds number, turbulent, separated and reattached flow around a fixed rectangular cylinder with chord-to-depth ratio equal to 5.

Some partial conclusions can be made: the overall simulated aerodynamic behaviour seems to agree well with the results in literature, even though the latter are sometimes dispersed; the POD analysis shows that, even though the 3D flow features are not negligible, the main phenomena which drive the aerodynamic forces remain 2D; the spanwise coherence of the pressure field qualitatively agrees with the results in literature, even though it is generally underestimated; the computational approach postprocessing facilities have been employed to shed light on some relationships between the vortex shedding and convection mechanisms, the instantaneous pressure field and the aerodynamic forces. In particular, homogeneous regions along the side surfaces have been proposed and the so-called “mean pressure recovery” region has been identified as the one that gives the most significant contribution to the lift force.

Further studies are encouraged to check the present proposal, to complete the knowledge of the main fluid flow phenomena that drives the section aerodynamics and to provide a complete data-base for validation and comparison purposes.

REFERENCES

[1] A. Okajima. Strouhal numbers of rectangular cylinders. *Journal of Fluid Mechanics*, **123**, 379–398, 1982.

[2] C. Norberg. Flow around rectangular cylinders: pressure forces and wake frequencies, *Journal of Wind Engineering and Industrial Aerodynamics*, **49**, 187–196, 1993.

[3] Y. Nakamura, Y. Ohya, S. Ozono, R. Nakamaya, Experimental and numerical analysis of vortex shedding from elongated rectangular cylinders at low Reynolds numbers 200-1000. *Journal of Wind Engineering and Industrial Aerodynamics*, **65**, 301–308, 1996.

[4] K. Hourigan, M. C. Thompson, B. T. Tan. Self-sustained oscillations in flows around long blunt plates. *Journal Fluid and Structures*, **15**, 387–398, 2001.

[5] B. T. Tan, M.C. Thompson, F. Hourigan. Flow past rectangular cylinders: receptivity to transverse forcing. *Journal of Fluid Mechanics*, **515**, 33–62, 2004.

[6] D.Yu, A.Kareem. Two-dimensional simulation of flow around rectangular prism. *Journal of Wind Engineering and Industrial Aerodynamics*, **62**, 131–161, 1996.

[7] D.Yu, A.Kareem. Parametric study of flow around rectangular prisms using LES. *Journal of Wind Engineering and Industrial Aerodynamics*, **77-78**, 653–662, 1998.

[8] K. Shimada, T. Ishihara. Application of a modified k-ϵ model to the prediction of aerodynamic characteristics of rectangular cross-section cylinders. *Journal of Fluid and Structures*, **16**, 465–485, 2002.

[9] M. Matsumoto, H. Shirato, K. Aaraki, T. Haramura, T. Hashimoto. Spanwise coherence characreristic of surface pressure field on 2D bluf bodies. *Journal of Wind Engineering and Industrial Aerodynamics*, **91**, 155–163, 2003.

[10] T. Tamura, I. Otha, K. Kuwahara. On the reliability of two-dimensional simulation for unsteady flows around a cylinder-type structure, *Journal of Wind Engineering and Industrial Aerodynamics*, **35**, 275–298, 1990.

[11] B.J. Vickery. Fluctuating lift and drag on a long cylinder of square cross-section in a smooth and in a turbulent stream. *Journal of Fluid Mechanics*, **25**, 481–494, 1966.

[12] R. J. Best, J. D. Holmes. Use of eigenvalues in the covariance integration method for determination of wind load effects. *Journal of Wind Engineering and Industrial Aerodynamics*, **13**, 359–370, 1983.

[13] J. D. Holmes. Analysis and synthesis of pressure fluctuations on bluff bodies using eigenvectors. *Journal of Wind Engineering and Industrial Aerodynamics*, **33**, 219–230, 1990.

[14] Y. Tamura, S. Suganuma, H. Kikuchi, K. Hibi. Proper Orthogonal Decomposition of random wind pressure field, *Journal of Fluids and Structures*, **13**, 1069–1095, 1999.

[15] K. F. Liaw. *Simulation of Flow around Bluff Bodies and Bridge Deck Sections using CFD*. PhD Thesis. University of Nottingham, 2005.

[16] A.Yoshizawa. Statistical theory for compressible shear flows with the application of subgrid modelling. *Physics of Fluids A*, **29**, 2152–2163, 1986.

[17] J. Smagorinsky. General circulation experiments with the primitive equations. I. The basic experiment. *Month. Weather Rev.*, **91**, 99–164, 1963.

[18] H.Jasak, H.G.Weller, A.D.Gosman. High resolution NVD differencing scheme for arbitrarily unstructured meshes. *International Journal for Numerical Methods in Fluids*, **31**, 431–449, 1999.

[19] G. Buresti. Vortex-shedding from bluff bodies. Proceeding of Wind effects on buildings and structures, Balkema, Rotterdam, 1998.

[20] A. Laneville, C.D. Williams. The effects of intensity and large scale turbulence on the mean pressure and drag coefficients of 2D rectangular cylinders. Proc. 5^{th} Int. Conference on Wind Effects on Building and Structures, Fort Collins, Colorado, July 8-14, 1979.

[21] Y. Nakamura, S. Ozono. The effects of turbulence on a separated and reattaching flow, *Journal of Fluid Mechanics*, **178**, 477–490, 1987.

[22] L. Bruno, D. Fransos. Edge degree-of-sharpness and integral length scale effects on the aerodynamics of a bridge deck. Proc. of the BBAA VI, Milano, Italy, July 20-24, 2008.